RESEARCH ARTICLE

An Extension of the Vector-Play Model to the Case of Magneto-Elastic Loadings

LUIZ GUILHERME DA SILVA[1,2,3], **ABDELLAHI ABDERAHMANE**[1,2], **MATHIEU DOMENJOUD**[1,2], **LAURENT BERNARD**[3], **AND LAURENT DANIEL**[1,2]

[1]Laboratoire de Génie Electrique et Electronique de Paris, CentraleSupélec, CNRS, Université Paris-Saclay, 91192 Gif-sur-Yvette, France
[2]Laboratoire de Génie Electrique et Electronique de Paris, CNRS, Sorbonne Université, 75252 Paris, France
[3]GRUCAD/EEL/CTC, Federal University of Santa Catarina (UFSC), Florianópolis 88040-900, Brazil

Corresponding author: Luiz Guilherme da Silva (luiz.dasilva@geeps.centralesupelec.fr)

ABSTRACT Accurate modeling of the coupling between mechanical and magnetic behavior is a key challenge for designing many electromagnetic devices. The requirements for such modeling are notably the ability to consider multiaxial configurations, thermodynamic consistency to allow the calculation of losses, and the implementability into structural analysis tools. So far, the modeling approaches available in the literature do not usually combine these three features simultaneously. In this paper, for the first time, the influence of mechanical stress on the magnetic hysteretic behavior is modeled through the association of a reversible simplified multiscale approach and a macroscopic energy-based magnetic hysteresis model in a vector-play form. A phenomenological description of the dissipation parameters under mechanical stress is proposed. The non-monotonic effect of tensile stress on the magnetic permeability is modeled using a second-order development in the magneto-elastic energy. Material parameters for both reversible and irreversible behavior are identified from experimental characterization under mechanical stress performed on a DC04 electrical steel. The experimental tests include anhysteretic and hysteretic measurements. Modeling results of the anhysteretic magnetic permeability, the coercive field, and the remanent induction under several levels of peak magnetic field and uniaxial mechanical stress are satisfactorily compared with those obtained experimentally. The model is shown to reasonably predict the hysteresis losses under tensile and compressive stress, as well as the response of the material under a complex magnetic field waveform with harmonic content.

INDEX TERMS Magneto-elastic behavior, hysteresis model, multiscale modeling, electrical steel.

I. INTRODUCTION

Mechanical stresses strongly influence the losses of magnetic materials. Such effects have been notably illustrated in electrical steels under uniaxial [1], [2] or biaxial [3] mechanical loadings. Due to this coupled behavior, the overall efficiency of electromagnetic devices can be altered by different mechanical stress sources, such as centrifugal forces [4], or shrink-fitting [5]. Several methods to model the coupled magneto-mechanical hysteretic behavior are presented in the literature and can be defined from either a macroscopic approach, a multiscale approach, or a combination of both.

In macroscopic models based on the classical scalar Jiles-Atherton (JA) approach - with anhysteretic behavior described by the Langevin function - the effects of stress on the magnetic behavior can be defined by an equivalent field incorporated in the effective field definition. Such an approach was used when uniaxial stress is applied along the magnetic field [6], [7], and when an angle between uniaxial stress and the magnetic field is considered [8]. The uniaxial mechanical limitation of these extensions of JA model can be overcome by considering the reversible behavior through the minimization of a Helmholtz free energy density, which is defined as a function of scalar invariants [9], [10]. In this approach, the scalar pinning parameter of the original JA model is replaced by a stress-dependent second-order

The associate editor coordinating the review of this manuscript and approving it for publication was Ladislau Matekovits[ID].

tensor [11], [12]. One drawback of this approach is the need for several measurements under stress to identify the parameters of the Helmholtz free energy function. Whereas the magnetic JA model is easy to implement, and its parameters are relatively easy to identify, some limitations were observed in the representation of asymmetric minor loops [13] and in the definition of the anhysteretic behavior as a function of an effective field, which results in non-physical reversible behavior [14].

Another macroscopic approach consists of a magneto-elastic extension of the classical scalar Preisach magnetic hysteresis model. It can be defined by introducing stress in the effective field definition [15], or considering the influence of stress in each hysteron operator [16], or in a probability distribution function [17]. The mathematical approach yields parameters that are difficult to identify from measurements.

A macroscopic magnetic hysteresis model based on an analogy with plasticity is presented in [18]. The magnetic energy is represented by analytical expressions. A switching surface with a radius determined by the coercive field captures the hysteretic behavior. However, complementary parameters fitted on experimental data are required to capture the first magnetization curve and asymmetric minor loops. Following this approach, in [19] a magneto-elastic thermodynamic framework is presented, and the main focus is on the response of magnetorheological elastomers with permanent magnets particles.

The second class of modeling concerns multiscale approaches. Three scales are considered: the magnetic domain, the single-crystal (or grain), and the representative volume element (RVE or polycrystal) scale [20]. Magnetic and mechanical quantities are defined at different scales through localization and homogenization schemes. Originally proposed to model the anhysteretic magneto-mechanical behavior [20], the approach shows good prediction capabilities with a clear protocol for parameter identification. A multiscale model with hysteresis is proposed in [21] with the inclusion of a hysteresis energy term in the domain free energy definition that depends on the previous state of magnetization. As pointed out in [22], the localization process in multiscale approaches can result in time-consuming finite element simulation of electromagnetic devices. This can be overcome, in the reversible case, by using simplified versions of the full multiscale approach. A simplification consists in considering an equivalent simplified crystallographic texture with a reduced number of crystal orientations, leading to a simplified texture multiscale model (STMSM) [22]. A further simplification consists in representing the macroscopic behavior using a fictitious equivalent single-crystal, similar to the Armstrong approach [23], leading to the so-called simplified multiscale model (SMSM) [24], [25]. This latter option, when limiting the number of possible domain orientations to six, can provide analytical formulas for the magneto-elastic behavior [26], [27].

In an analogous multiscale approach called assembled domain structure model (ADSM), each ADSM is made of a simplified domain structure model (SDSM) formed by six domains. The magnetization direction of each domain is related to the easy axes of the material. A minimization of the energy balance (which comprises a magneto-elastic term) in a SDSM structure results in the magnetization state [28]. The hysteresis effects are reproduced by considering a pinning field defined by a Gaussian distribution [29].

The last class of magneto-mechanical hysteresis models consists of a combination approach: the reversible behavior is modeled with a magneto-mechanical multiscale approach, and the magnetic hysteresis is considered from a macroscopic description. In this case, examples are the combination of the full multiscale approach and Hauser model [30], the SMSM with the magnetic JA model [22], [31], [32], and the analytical multiscale model with the Kádár product model [33] or with the JA model [34]. Hysteresis effects are considered in the Armstrong model by defining a macroscopic energy dissipation term related to the defects of a material, which constrains the domain wall motion [35]. Improvements of this approach to represent asymmetric minor loops and an extension to consider variable stress under constant magnetic field are presented in [36].

These three classes here introduced contemplate only some examples of magneto-mechanical hysteresis models. Besides these classes, phase-field approaches can be highlighted. This modeling aims to describe the spatial and temporal evolution of magnetic domains in a microstructure. Numerical methods are used to minimize an energy function related to the domain wall motion of a discretized ferromagnetic material [37], [38]. This approach gives detailed information about the microstructure of a ferromagnetic material under magnetic and mechanical loadings. When the macroscopic response is sought, this modeling increases the computational cost.

Although many hysteretic magneto-elastic modeling approaches are available in the literature, as described above, none of them simultaneously combines three key features for the numerical analysis of electromagnetic devices. The first one is the ability to consider fully multiaxial loadings as encountered in practical applications, the second is thermodynamic consistency to compute losses accurately, and the last is the implementation into numerical analysis tools, which requires low computation time for behavior evaluation. In this paper, for the first time, a combination of a SMSM with an energy-based magnetic hysteresis model in a vector-play form [39], [40] is proposed. This rate-independent magnetic hysteresis model is based on an energetic description at the macroscopic scale and defined directly in a vector form. The association with the SMSM allows multiaxial stress configurations. The parameters are evaluated from a magneto-elastic characterization performed on DC04 steel under compression and tension, and the performance of the model is evaluated on a different set of experimental data.

II. MAGNETO-ELASTIC MODEL

The thermodynamics basis of the coupled magneto-elastic model is addressed in this section with a distinction between reversible and irreversible processes. The relationship between magnetic induction $\vec{B}$, magnetic field $\vec{H}$, magnetization $\vec{M}$, magnetic polarization $\vec{J}$ and vacuum permeability μ_0 is expressed as:

$$\vec{B} = \mu_0 \left(\vec{H} + \vec{M} \right) = \mu_0 \vec{H} + \vec{J}. \tag{1}$$

A. THERMODYNAMICS ASPECTS

In the framework of continuum thermodynamics, the first law of thermodynamics in a ferromagnetic material at the macroscopic scale can be written as [40]:

$$\dot{u} = \vec{H} \cdot \dot{\vec{B}} + \sigma : \dot{\epsilon} - \operatorname{div} \vec{q}, \tag{2}$$

$\dot{u}$ is the time-derivative of the internal energy density, the dot product $\vec{H} \cdot \dot{\vec{B}}$ represents the magnetic power density, the double-contraction product $\sigma : \dot{\epsilon}$ between the second-order tensors of mechanical stress σ and strain rate $\dot{\epsilon}$ represents the mechanical power density, and $\vec{q}$ the heat flux. The second law of thermodynamics can be expressed as [41]:

$$T\dot{s} \geq -\operatorname{div}\vec{q} + \operatorname{grad} T \cdot \left(\frac{\vec{q}}{T} \right), \tag{3}$$

with s the entropy and T the temperature. Defining the Helmholtz free energy density as $f \equiv u - Ts$, combining (1), (2) and (3), and neglecting spatial and temporal thermal variations, the Clausius-Duhem inequality (CDI) for the magneto-mechanical case writes:

$$D = \vec{H} \cdot \dot{\vec{J}} + \sigma : \dot{\epsilon} - \dot{f} \geq 0, \tag{4}$$

with D the dissipation. The term $\mu_0 \vec{H} \cdot \dot{\vec{H}}$ is omitted because, in general, it is negligible in comparison to the contribution of $\vec{H} \cdot \dot{\vec{J}}$ to the magnetic power density. A summary of the thermodynamics laws and approximations considered is presented in Table 1.

TABLE 1. Summary of the thermodynamic laws for the magneto-elastic case.

1st law	$\dot{u} = \vec{H} \cdot \dot{\vec{J}} + \sigma : \dot{\epsilon} - \operatorname{div}\vec{q}$ Considering $\vec{H} \cdot \dot{\vec{B}} = \vec{H} \cdot \dot{\vec{J}}$
2nd law	$T\dot{s} \geq -\operatorname{div}\vec{q} + \operatorname{grad} T \cdot \left(\dfrac{\vec{q}}{T} \right)$
CDI	$D = \vec{H} \cdot \dot{\vec{J}} + \sigma : \dot{\epsilon} - \dot{f} \geq 0$ Considering $\dot{T} = 0$, $\operatorname{grad} T = 0$

Considering only the reversible behavior ($D = 0$), the Legendre transformation allows writing (4) as a function of
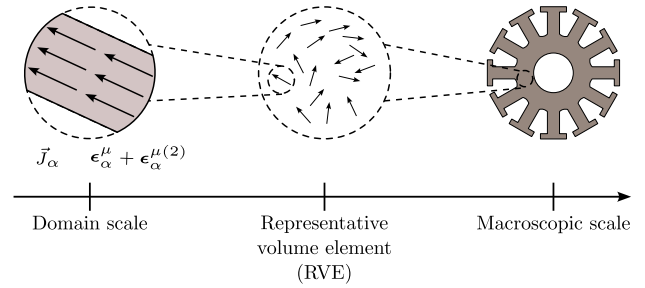

FIGURE 1. Scales involved in the reversible modeling.

the time-derivative of the Gibbs free energy $\dot{g}$:

$$\dot{g} = -\dot{\vec{H}} \cdot \vec{J} - \dot{\sigma} : \epsilon. \tag{5}$$

B. REVERSIBLE BEHAVIOR

The reversible behavior is modeled using a simplified multiscale approach [25]. The scales considered are represented in Figure 1. In this work, we are interested in modeling the behavior of the RVE. The following assumptions are made: (a) the material behavior is isotropic, (b) demagnetizing effects are negligible, and (c) both applied magnetic field and mechanical stress are homogeneous at the domain scale (denoted by α).

In a domain family with direction $\vec{\alpha}$, the polarization $\vec{J}_\alpha$ is:

$$\vec{J}_\alpha = \mu_0 M_s \vec{\alpha} = \mu_0 M_s \left[\alpha_1 \; \alpha_2 \; \alpha_3 \right]^t, \tag{6}$$

with M_s the saturation magnetization. The magnetostriction strain ϵ_α^μ for isotropic behavior is:

$$\epsilon_\alpha^\mu = \frac{3}{2}\lambda_s \left(\vec{\alpha} \otimes \vec{\alpha} - \frac{1}{3}\boldsymbol{I} \right), \tag{7}$$

where λ_s denotes the maximum magnetostriction strain, $\otimes$ represents the tensor product, and $\boldsymbol{I}$ is the second-order identity tensor. The energy variation dg_α for a time step dt at the domain scale is written [42]:

$$dg_\alpha = -\vec{J}_\alpha \cdot d\vec{H} - \epsilon_\alpha : d\sigma. \tag{8}$$

with ϵ_α the total strain at the domain scale. The magnetic part of the Gibbs free energy is defined by the integration over the magnetic field path:

$$g_\alpha^{mag} = -\vec{J}_\alpha \cdot \vec{H}. \tag{9}$$

Considering small perturbations: $\epsilon_\alpha = \epsilon_\alpha^e + \epsilon_\alpha^\mu$, with ϵ_α^e the elastic strain. Supposing uniform strain in the single-crystal, the magneto-elastic part of the Gibbs free energy is written by integration over the stress path [42]:

$$g_\alpha^{el(1)} = -\epsilon_\alpha^\mu : \sigma. \tag{10}$$

It was shown in earlier works that the effect of stress on magnetization is non-monotonic [30], [42] and this simplified approach does not capture such a tendency. This drawback can be solved by adding a stress-dependent demagnetizing term in the energy balance [30], or by adding a second order

term - quadratic in stress - in the magneto-elastic energy definition [42]. We choose here this second option. The magneto-elastic energy is therefore defined as:

$$
\begin{aligned}
g_\alpha^{el} &= g_\alpha^{el(1)} + g_\alpha^{el(2)} \\
&= -\boldsymbol{\sigma} : \boldsymbol{\epsilon}_\alpha^\mu - \frac{3}{2}\lambda_s'\sigma_{eq}^2 \left(\vec{\alpha} \otimes \vec{\alpha} - \frac{1}{3}\boldsymbol{I} \right) : \left(\vec{h} \otimes \vec{h} \right),
\end{aligned} \quad (11)
$$

with $g_\alpha = g_\alpha^{mag} + g_\alpha^{el}$. In this definition, the second-order magnetostriction constant λ_s' is introduced and the equivalent stress σ_{eq} [43] is written in terms of $\vec{h} = \vec{H}/\|\vec{H}\|$ and the deviatoric part of $\boldsymbol{\sigma}$:

$$
\sigma_{eq} = \frac{3}{2}\vec{h}^t \left(\boldsymbol{\sigma} - \frac{1}{3}\operatorname{tr}(\boldsymbol{\sigma})\boldsymbol{I} \right) \vec{h}. \quad (12)
$$

The magnetostriction strain is composed of the sum of (7) with a second-order magnetostriction strain $\boldsymbol{\epsilon}_\alpha^{\mu(2)}$:

$$
\boldsymbol{\epsilon}_\alpha^{\mu(2)} = -\frac{\partial g_\alpha^{el(2)}}{\partial \boldsymbol{\sigma}}. \quad (13)
$$

Considering a particular case under uniaxial stress $\sigma_{eq} = \sigma_{11}$ applied along the magnetic field direction $\vec{h} = [1\ 0\ 0]^t$, the only non-null component of $\boldsymbol{\epsilon}_\alpha^{\mu(2)}$ is:

$$
\epsilon_{\alpha_{11}}^{\mu(2)} = \frac{3}{2} \left(2\lambda_s'\sigma_{11} \right) (\alpha_1^2 - 1/3). \quad (14)
$$

Therefore, introducing a second-order term in the magneto-elastic energy results in a magnetostriction strain that is stress-dependent. This allows capturing the non-monotonic effect of tensile stress on the magnetic behavior [42], [44]. λ_s' can be defined as (see Appendix A):

$$
\lambda_s' = -\frac{\lambda_s}{2\sigma_m}, \quad (15)
$$

where σ_m is the value of the applied stress corresponding to the maximum magnetic permeability. Combining (11) and (15), the elastic part of the Gibbs free energy is:

$$
g_\alpha^{el} = -\boldsymbol{\sigma} : \boldsymbol{\epsilon}_\alpha^\mu + \frac{\sigma_{eq}^2}{2\sigma_m}\boldsymbol{\epsilon}_\alpha^\mu : \left(\vec{h} \otimes \vec{h} \right). \quad (16)
$$

The volume fraction p_α of a domain family with direction $\vec{\alpha}$ is evaluated using a Boltzmann relation [45]:

$$
p_\alpha = \frac{\exp\left(-A_s\, g_\alpha \right)}{\sum_\alpha \exp\left(-A_s\, g_\alpha \right)}, \quad (17)
$$

where the parameter A_s is proportional to the initial susceptibility χ_0 of the stress-free anhysteretic curve [20]:

$$
A_s = \frac{3\chi_0}{\mu_0 M_s^2}. \quad (18)
$$

In this simplified approach, the domain orientations are defined from a discretization of a unit sphere [46]. The macroscopic polarization and macroscopic strain are:

$$
\vec{J} = \sum_\alpha p_\alpha \vec{J}_\alpha \quad (19a)
$$

$$
\boldsymbol{\epsilon} = \sum_\alpha p_\alpha \boldsymbol{\epsilon}_\alpha. \quad (19b)
$$

C. IRREVERSIBLE PROCESS AND VECTOR-PLAY MODEL

In a reversible framework at a macroscopic scale, a reversible magnetic field $\vec{H}_{rev}$ and a reversible stress $\boldsymbol{\sigma}_{rev}$ are defined:

$$
\vec{H}_{rev} \equiv \frac{\partial f}{\partial \vec{J}} \quad (20)
$$

$$
\boldsymbol{\sigma}_{rev} \equiv \frac{\partial f}{\partial \boldsymbol{\epsilon}}. \quad (21)
$$

Combining (20) and (21) with the Clausius-Duhem inequality (4) yields:

$$
D = (\vec{H} - \vec{H}_{rev}) \cdot \dot{\vec{J}} + (\boldsymbol{\sigma} - \boldsymbol{\sigma}_{rev}) : \dot{\boldsymbol{\epsilon}} \geq 0. \quad (22)
$$

In the dissipative framework, an irreversible field $\vec{H}_{irr} = (\vec{H} - \vec{H}_{rev})$ and an irreversible stress $\boldsymbol{\sigma}_{irr} = (\boldsymbol{\sigma} - \boldsymbol{\sigma}_{rev})$ are introduced. A simplification consists in considering mechanical stress only in a reversible way, and as a result $\boldsymbol{\sigma}_{irr} = \boldsymbol{0}$.

The dissipation is modeled by analogy with a mechanical dry-friction system [39]. The defects that pin domain walls at specific positions are represented by a pinning field κ, a positive scalar in the isotropic case. The dissipation writes:

$$
D = \kappa\|\dot{\vec{J}}\| = \vec{H}_{irr} \cdot \dot{\vec{J}}. \quad (23)
$$

As in the reversible case - where a relation between $\vec{H}_{rev}$ and f was defined - $\vec{H}_{irr}$ can be written as a function of the partial derivative of D. Since D is not differentiable at $\dot{\vec{J}} = \vec{0}$, the subdifferential of a convex function is considered [39], [47]:

$$
\frac{\partial D}{\partial \dot{\vec{J}}} = \begin{cases} \vec{H}_{irr}, \|\vec{H}_{irr}\| \leq \kappa & \text{if } \dot{\vec{J}} = \vec{0} \\ \vec{H}_{irr} = \kappa \dfrac{\dot{\vec{J}}}{\|\dot{\vec{J}}\|} & \text{otherwise.} \end{cases} \quad (24)
$$

This implies that for $\|\vec{H}_{irr}\| < \kappa$ the polarization $\vec{J}$ will remain constant until $\|\vec{H}_{irr}\| = \kappa$ [47]. From the previous definitions:

$$
(\vec{H} - \vec{H}_{rev} - \vec{H}_{irr}) = \vec{0}. \quad (25)
$$

The pinning parameter in real materials can be represented by a statistical distribution of pinning fields κ^k with $N-$ dry-friction systems (or cells) with normalized weights ω^k that verify $\sum_{k=1}^N \omega^k = 1$ [40]. At each cell k, the polarization $\vec{J}^k(\vec{H}_{rev}^k, \boldsymbol{\sigma})$ and strain $\boldsymbol{\epsilon}^k(\vec{H}_{rev}^k, \boldsymbol{\sigma})$ are related to the homogenized quantities:

$$
\vec{J} = \sum_{k=1}^N \omega^k \vec{J}^k(\vec{H}_{rev}^k, \boldsymbol{\sigma})
$$

$$
\boldsymbol{\epsilon} = \sum_{k=1}^N \omega^k \boldsymbol{\epsilon}^k(\vec{H}_{rev}^k, \boldsymbol{\sigma}). \quad (26)
$$

The following simplification can be made: the direction of $\vec{H}_{irr}$ is written in terms of the reversible field at the previous time step $\vec{H}_{rev(p)}^k$. This results in a vector-play model [39].
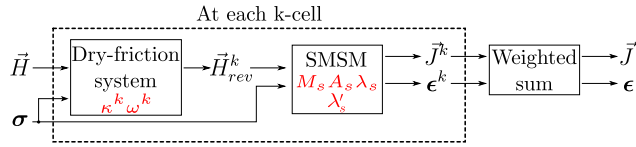
FIGURE 2. Principle of the stress-dependent hysteresis model. The material parameters are indicated in red.

Using this approximation, the explicit update procedure of $\vec{H}_{rev}^k$ at each cell is:

$$\vec{H}_{rev}^k = \begin{cases} \vec{H}_{rev(p)}^k & \text{if } \|\vec{H} - \vec{H}_{rev(p)}^k\| \leq \kappa^k \\ \vec{H} - \kappa^k \dfrac{\vec{H} - \vec{H}_{rev(p)}^k}{\|\vec{H} - \vec{H}_{rev(p)}^k\|} & \text{otherwise.} \end{cases}$$

(27)

The field $\vec{H}_{rev}^k$ and $\boldsymbol{\sigma}$ are the inputs of the SMSM. $\vec{J}^k(\vec{H}_{rev}^k, \boldsymbol{\sigma})$ and $\boldsymbol{\epsilon}^k(\vec{H}_{rev}^k, \boldsymbol{\sigma})$ are the outputs. $\vec{J}$ and $\boldsymbol{\epsilon}$ are then defined by (26). $\vec{B}$ is given by (1). A simplified schematic of the algorithm is presented in Fig. 2.

III. EXPERIMENTAL SETUP

The apparatus used to carry out the magneto-mechanical characterization of a sample of DC04 steel (250 mm x 20 mm x 2 mm) under uniaxial stress is detailed in [48] and shown in Fig. 3. The mechanical setup is composed of a tension/compression machine Zwick/Roell Z030 with the possibility to control in force or displacement. A force control is used with a resolution and accuracy of 0.2 N $\pm$ 0.06%, and force measurements are performed using a 10 kN load cell (strain gauge sensor TC-LC010kN).

The magnetic setup is composed of two U-shaped Fe-Si yokes to ensure the closure of the magnetic flux. A Kepco 72-14MG amplifier, that can deliver 14 A and 72 V with 0.2% accuracy, supplies current to an excitation coil (28 turns) positioned around the sample. The current is measured with a LA 125-P transducer with 0.6% accuracy. A Teslameter FM302 and a transverse Hall probe 20 mT AS-VTP, which can operate from DC to 1 kHz, measure the magnetic field with an accuracy of 0.5 % and measured noise of 19 A/m in the range of 0 - 15.9 kA/m. The time integration of the induced voltage of a B-coil (85 turns) wound around the sample (measurement area of Fig. 3) results in the measured induction with measured noise of about 0.1 mT with accuracy of 0.2% [48].

The magnetostriction strain is measured with a strain gauge rosette glued on the measurement area surface (Fig. 3) of the sample. The signal is amplified with a 4-channel strain gauge conditioner Vishay 2120 B with about 0.5% of accuracy and measured noise of about 10^{-6}. A DS 1006 dSPACE processor board performs the acquisition and control of signals with a sampling frequency of 50 kHz. More information on the control and acquisition system can be found in [48]. A measurement reproducibility error is found to be about 0.5% in the magnetic field and 0.3% in the induction.
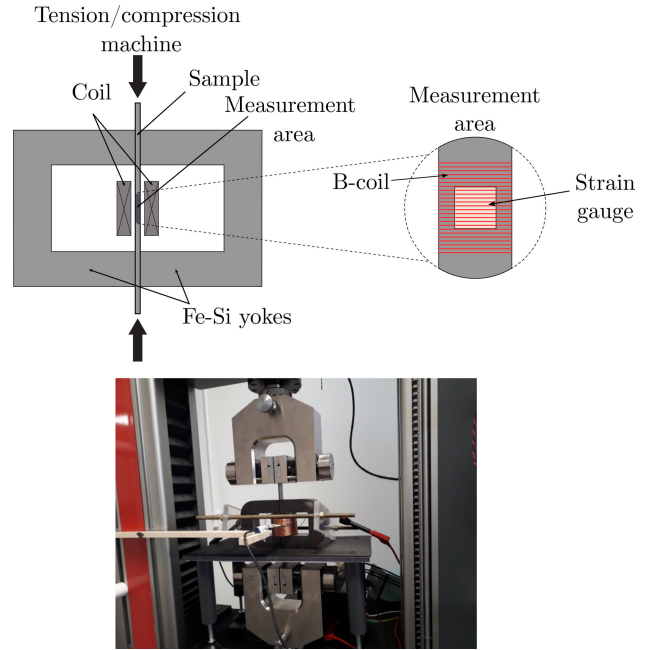

FIGURE 3. Experimental setup for magnetic characterization under uniaxial stress.

The procedure to measure the anhysteretic magnetic behavior is detailed in [49]. The controlled current is set as an exponentially decaying sine wave, defined with a frequency of 1 Hz, superimposed to a bias level. This approach is repeated at several bias levels and under mechanical compressive (-) and tensile (+) uniaxial stresses that vary between -100 MPa and 100 MPa. The stress levels are defined to be below the yield stress of the sample (120 MPa) and the Euler buckling critical load estimated as -296 MPa.

The hysteresis measurements are performed at the same typical levels of stress and electric current, but the frequency of the electrical loading is reduced to 25 mHz. Indeed, it was observed that it is the frequency at which the quasi-static regime is attained (see Appendix B). The procedure to correct the drift in the measured induction is presented in Appendix C. Table 2 shows the quantities involved in the characterization process.

The magnetic quantities H_c (coercive field) and B_r (remanent induction) are evaluated by a linear regression around the point of interest - $B = 0$ for H_c and $H = 0$ for B_r. A post-processing filtering is applied to the measurements using a 50-point moving average on the cycle. The error bars take into account the noise and reproducibility presented before. Measurement results are discussed in section V when compared to modeled estimates.

IV. IDENTIFICATION OF MATERIAL PARAMETERS

The magneto-elastic model is entirely defined by the parameters of the anhysteretic behavior, here based on the SMSM, and the probability distribution of pinning field $\omega(\kappa)$. The parameters are evaluated from anhysteretic and hysteretic characterizations under uniaxial stress.

TABLE 2. Summary of the measured quantities during experiments.

	Loading	Measurements
Anhysteretic	Stress $\sigma = [-100{:}20{:}100]$ MPa Bias H-field: 20 values between 0 and 3000 A/m	Induction $B^{anh}(H^{anh}, \sigma)$
Hysteretic	Stress $\sigma = [-100{:}20{:}100]$ MPa Peak field H_{peak}: 15 values between 140 A/m and 6800 A/m	Induction $B(H, \sigma)$ Longi. and transv. magnetostriction $\epsilon_l^\mu(H, \sigma)$ $\epsilon_t^\mu(H, \sigma)$
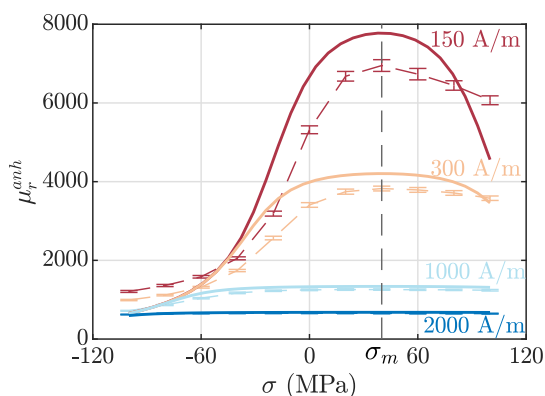
FIGURE 4. Comparison of measured (error bars) and modeled (solid lines) anhysteretic relative magnetic permeability for different values of applied magnetic field. The maximum anhysteretic permeability is observed at $\sigma_m = 40$ MPa.
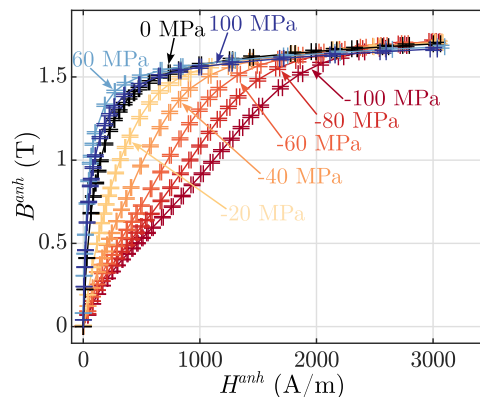
TABLE 3. Parameters of the SMSM.

M_s (A/m)	λ_s (ppm)	λ_s' (ppm/MPa)	A_s (m³/J)
$1.39\,10^6$	5.5	$-6.9\,10^{-2}$	$1.4\,10^{-2}$
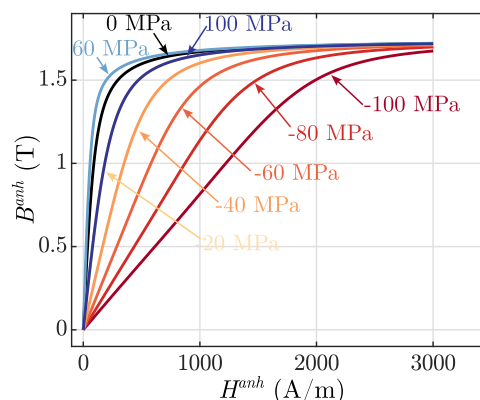
FIGURE 5. Effect of uniaxial stress on the anhysteretic behavior: Measurements (top) and model (bottom).

A. REVERSIBLE PARAMETERS

The reversible parameters M_s, λ_s, and χ_0 are identified from anhysteretic characterization without applied stress. M_s is the maximum magnetization measured on the stress-free M-H curve. λ_s is the maximum longitudinal magnetostriction strain obtained on the stress-free magnetostriction curve. χ_0 is the slope, at $H = 0$, of the anhysteretic stress-free M-H curve. A_s is calculated from χ_0 by using (18).

Fig. 4 presents the anhysteretic relative magnetic permeability μ_r^{anh} as a function of the applied stress for different values of the magnetic field. A non-monotonic effect of tensile stress on the reversible behavior is observed. Such non-monotonicity justifies the use of a second-order term in the magneto-elastic energy. This approach introduces an additional material parameter λ_s' (see (11)) which can be identified from (15).

The identified reversible parameters are presented in Table 3. The modeled anhysteretic behavior results in Fig. 5 (bottom) and shows a good agreement with the measurements in Fig. 5 (top). Fig. 4 shows that the SMSM with a second-order term can capture the reversible behavior and the non-monotonic effect. Differences become apparent, especially for tensile stress of 100 MPa, where the model underestimates the relative permeability at low field. Such a tendency is inevitable with the proposed description (second-order

elastic energy term), which imposes the permeability curve to be symmetric with respect to σ_m, as shown in Appendix A. A possibility to improve this drawback would be using a stress-dependent demagnetizing term in the free energy, as proposed in [30], instead of or as a complement to the second-order approach. Another option would be introducing higher order terms in the elastic energy, to the price of additional material parameters.

B. DISSIPATIVE PARAMETERS

Considering a magnetic case with applied field along $\vec{h} = [1\ \ 0\ \ 0]^t$, an identification method of $\omega(\kappa)$ is presented in [50], [51]. This procedure is based on the homogenization of reversible field, where it is defined an auxiliary function $F(H)$ (see Appendix D). The second derivative of $F(H)$ is the probability distribution $\omega(\kappa)$. The identification of $F(H)$ (as explained in Appendix D) can be performed from a set of measured H_c under increasing peak magnetic fields H_{peak}. These experimental measurements are presented in Fig. 6 for the stress-free case. This curve is extrapolated outside the
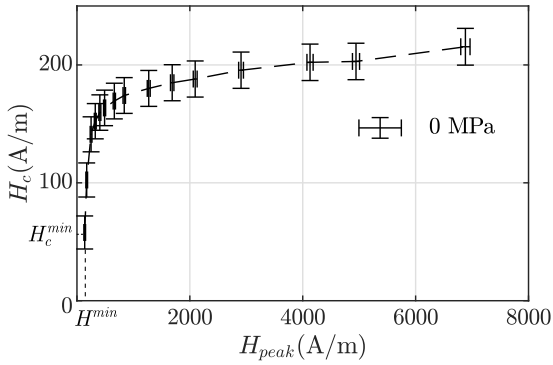
FIGURE 6. Experimental measurements of coercive field under increasing magnetic field for the stress-free case.
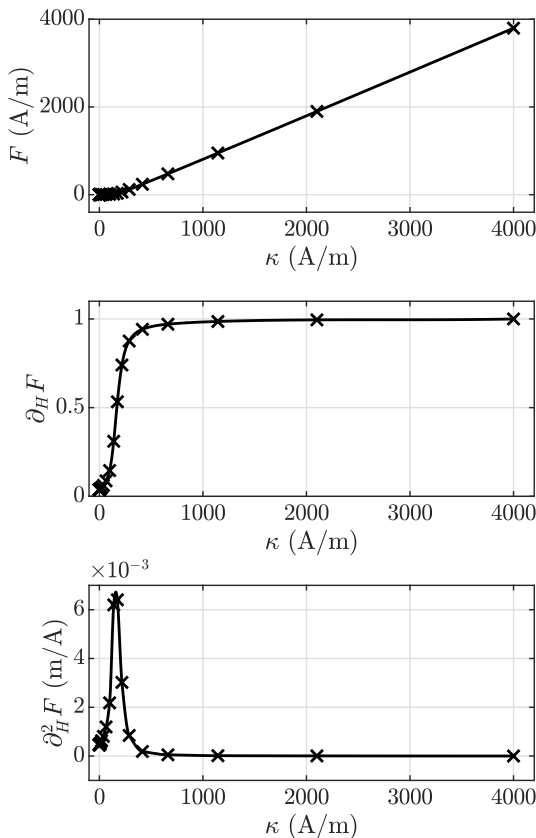

FIGURE 7. Identified auxiliary function for the stress-free case, first and second derivatives that represent the pinning field cumulative distribution and probability distribution, respectively.

FIGURE 8. Hysteresis curves under uniaxial stress: Measurements (top) and model (bottom).
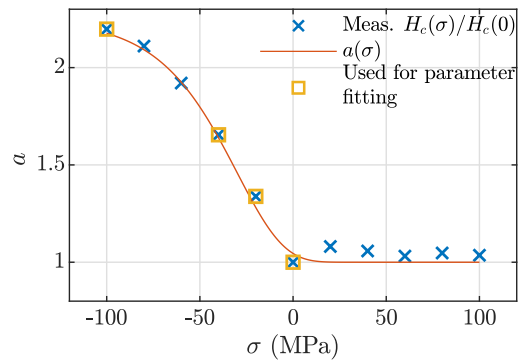
FIGURE 9. Function a(σ) at several stress levels.

measured range using (28) [51]:

$$H_c(H) = H_c^{min} \left(\frac{H}{H^{min}} \right)^2 \quad \text{if } H < H^{min}, \qquad (28)$$

where H_c^{min} is the lower measured coercive field on the corresponding peak magnetic field H^{min}. The identified $F(H)$ and its derivatives $\partial_H F(H)$ and $\partial_H^2 F(H)$, are presented in Fig. 7. The derivatives are evaluated with a finite differences method. The non-zero component for $\kappa(0)$ represents the bending of Bloch walls [39]. The continuous probability distribution is then discretized into 25 cells (see (45) in Appendix D).
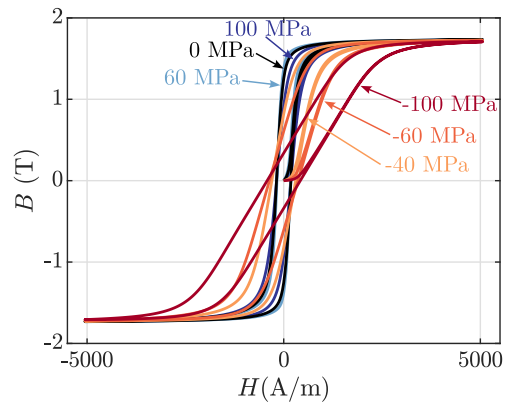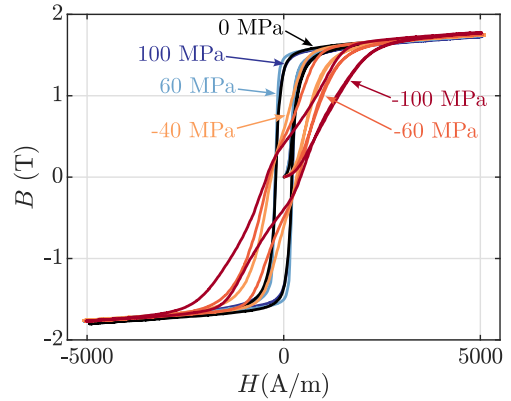
An applied compression increases the coercive field, as observed in the measured hysteresis curves of Fig. 8 (top). The pinning parameter κ is directly related to the coercive field. We propose to model the stress dependence of dissipation parameters as follows: starting from the identified discrete pinning field distribution for 0 MPa, the weight ω is kept constant under stress. The pinning field $\kappa(\sigma)$ evolves as:

$$\kappa(\boldsymbol{\sigma}) = a(\boldsymbol{\sigma})\kappa(\mathbf{0}), \qquad (29)$$

with $\kappa(\mathbf{0})$ the identified pinning field for 0 MPa, and $a(\boldsymbol{\sigma})$ a function that is fitted in order to match with the measured
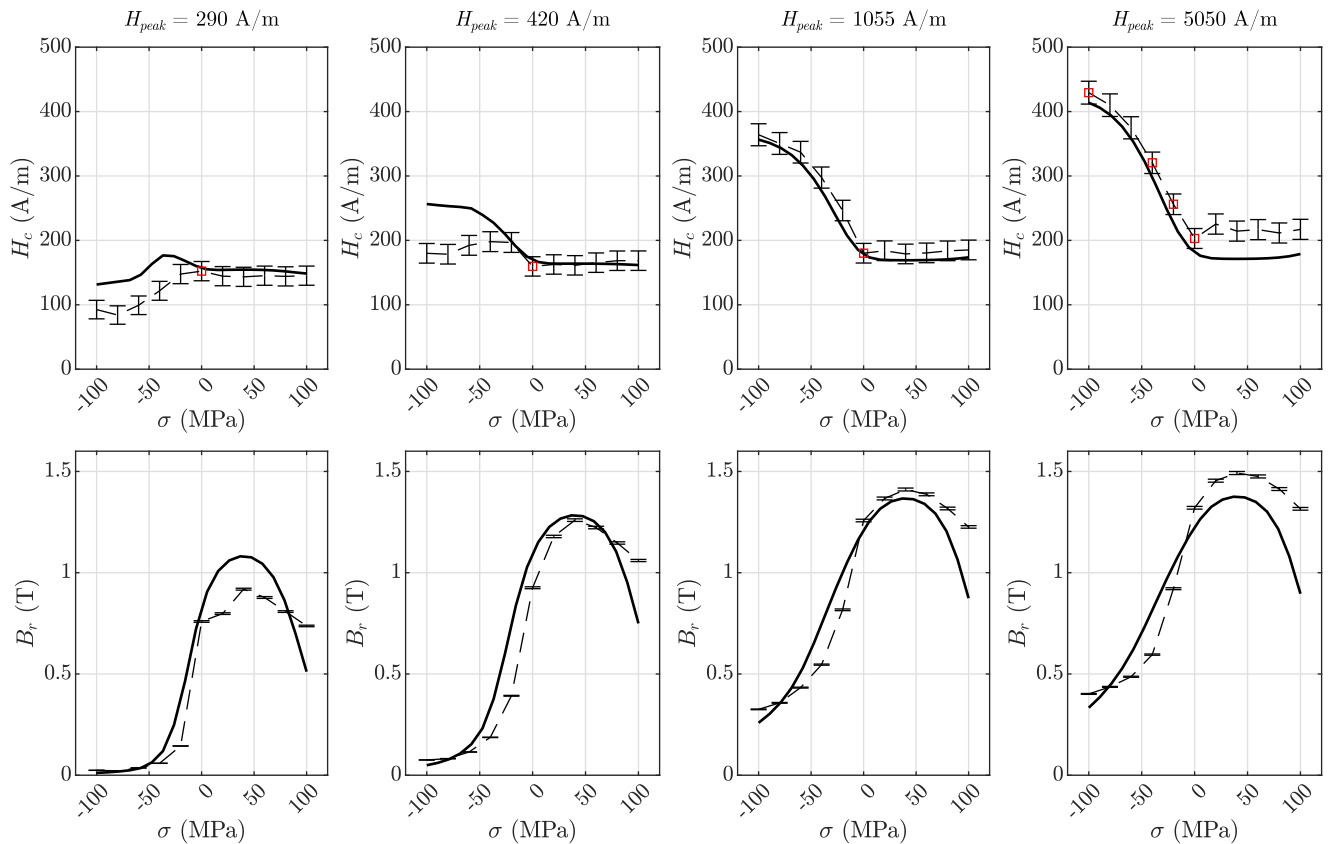
FIGURE 10. Comparison of measured (error bars) and modeled results (solid lines) of coercive field (top) and remanent induction (bottom) as a function of uniaxial stress and under various peak magnetic fields. The red boxes (top) indicate the fitted values.

TABLE 4. Fitted parameters for a(σ).

a_1	a_2	a_3 (MPa^{-1})
1.25	1.2	0.04

$H_c(\boldsymbol{\sigma})/H_c(\mathbf{0})$. This coercive field characteristic under stress is presented in Figure 9 in the case of uniaxial stress applied parallel to the magnetic field direction. It can be noted an exponential behavior of H_c under compression and a close to constant behavior under tension. For other materials, such as Fe-Si [52], the exponential tendency of the coercive field under compression is also observed.

A phenomenological description of $a(\boldsymbol{\sigma})$ is then defined by:

$$a(\boldsymbol{\sigma}) = a_1 \exp\left(-\exp(a_2 + a_3\sigma_{eq})\right) + 1, \qquad (30)$$

with σ_{eq} the equivalent stress (12). The parameters a_1, a_2 and a_3 are fitted from four measured coercive fields under 0 MPa, -20 MPa, -40 MPa and -100 MPa, respectively, by using the Curve Fitting Toolbox of Matlab. The identified parameters are presented in Table 4. Fig. 9 shows that (30) is appropriate to represent the measured coercive field characteristic under uniaxial mechanical loading.

The identification procedure of the dissipation parameters can be summarized as follows: from the stress-free curve of coercive field with increasing magnetic field, the method

presented in [50], [51] allows identifying $\omega(\kappa(\mathbf{0}))$. By using standard measurements of coercive field under stress, the function $a(\boldsymbol{\sigma})$ is fitted, and so the dependence $\kappa(\boldsymbol{\sigma})$ of (29) is defined.

V. VALIDATION
The proposed magneto-elastic model results in the hysteresis curves presented in Fig. 8 (bottom), and the tendency of slant under compression - as observed in measurements of Fig. 8 (top) - is captured by the simulation. However, the model does not reproduce inflections in the hysteresis curve - more evident under -100 MPa. This measured behavior is attributed to the crystallographic texture, whereas in this proposed model, only an equivalent single crystal representing the macroscopic behavior is considered. A simplified texture multiscale model (STMSM) [22] may overcome this limitation, but it is not treated in this work.

Fig. 10 (top) presents a comparison of the modeled coercive field with the measured symmetric minor loops under uniaxial stress. It is insisted here that the validation is performed by comparison to the experiments that have not been used for identification purposes. For the sake of clarity, the measured values used for identification are explicitly labeled in Fig. 10. Differences are observed in the major loop under tensile stress (25% for 20 MPa and 5050 A/m) but the general
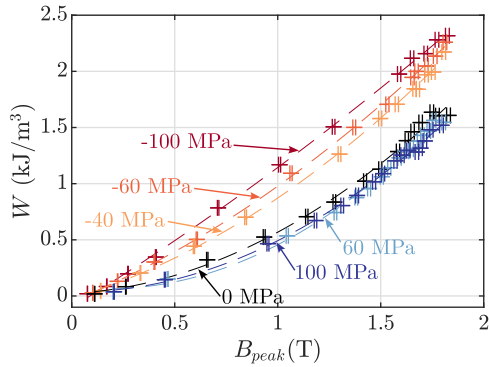
FIGURE 11. Measured hysteresis losses as a function of peak induction for different uniaxial stress.
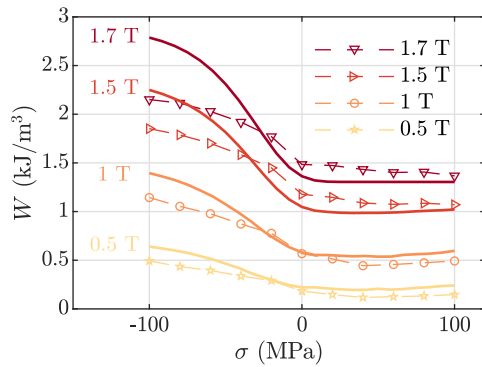

FIGURE 12. Prediction of hysteresis losses as a function of uniaxial stress (solid lines). The experimental results (markers) are evaluated using measured data from Fig. 11 and polynomial interpolation.
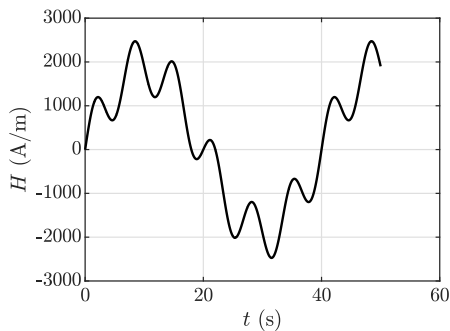

FIGURE 13. Applied magnetic field signal to simulate asymmetric minor loops.

behavior under stress is captured by the simulation. The second-order term in the magneto-elastic energy definition (11) allows the representation of the non-monotonic effect of tensile stress on the remanent induction B_r as seen in Fig. 10 (bottom).

The measured hysteresis losses under uniaxial stress as a function of the maximum induction are shown in Fig. 11, where the usual behavior - an increase of losses with increasing compression [1] - is observed.

The prediction of hysteresis losses under stress is plotted in Fig. 12 by numerical integration of the surface of each hysteresis loop and is presented as a function of the maximum
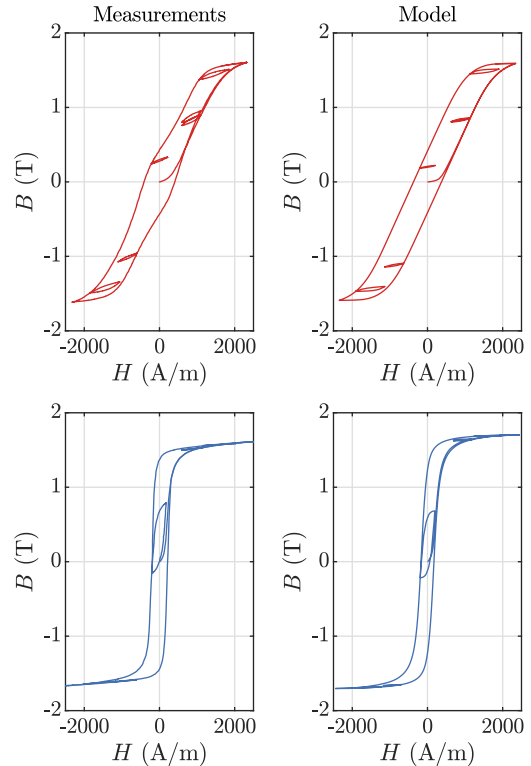

FIGURE 14. Hysteresis curves under uniaxial stress and considering the magnetic field waveform of Fig. 13. Stress levels from top to bottom: -80 MPa and 80 MPa.

induction level. This calculation is a blind validation of the modeling approach since no loss measurement was used for material parameter identification. The modeling results show that the tendency to increase losses under compression is reproduced. Significant differences are seen mainly in the major loop under high compression. As already discussed, the SMSM does not consider the inflections in hysteresis curves under compression, which explains the difference of about 30% for the worst case (-100 MPa and 1.7 T).

Fig. 13 shows a magnetic field waveform that allows producing a material response with asymmetric minor loops presented in Fig. 14. The comparison of measurements and model is presented in Fig. 14 for two levels of uniaxial stress. Under a tensile stress of 80 MPa, because the hysteresis curve is less slanted, only one asymmetric minor loop is clearly visible, with the others remaining in a region above 1000 A/m. Again, this comparison is independent of the identification process, so it can serve as a validation for the model. A good agreement between the model and experiment is observed, despite the harmonic content of the H waveform.

VI. CONCLUSION
In this paper, an extension of the energy-based vector-play magnetic hysteresis model has been proposed for the first time in order to incorporate the effect of stress on magnetization. This extension essentially consists of the association of the vector-play model with an anhysteretic sim-

plified multiscale approach. This combination results in a magneto-elastic vector model applicable to multi-axial stress configurations. Stress-dependent dissipation parameters can be identified from a few measurements, mostly under compression. An accurate prediction of coercive field and remanent induction under stress were observed when compared to experimental measurements performed on electrical steel. The inclusion of a second-order development in the magneto-elastic energy enables capturing the non-monotonic evolution of the magnetic permeability under stress.

The magneto-elastic model can predict the general behavior of hysteresis losses under mechanical loadings from a small set of parameters and reasonably reproduce asymmetric minor loops. This strategy can be an interesting approach in the coupled magneto-elastic finite element simulation of electromagnetic devices subject to multi-axial stress and fed from a PWM (pulse width modulation) power converter. The proposed model is fully multi-axial. However, it has been validated so far only for uniaxial stress conditions. Validation under complex configurations, such as rotating fields and/or biaxial mechanical loadings, is required. Moreover, only static mechanical loadings have been considered. The extension to dynamic mechanical loading is necessary to cover the piezomagnetic behavior case. Such investigations will be considered in future works.

APPENDIX A
IDENTIFICATION OF THE MAGNETOSTRICTION CONSTANT λ_s'

The identification of the second-order magnetostriction constant λ_s' is obtained from the analysis of the analytical expression of the anhysteretic relative magnetic permeability $\mu_r^{anh}(\sigma)$. Considering $\mu_r^{anh}(\sigma)$ for isotropic materials, and the magnetic field in the direction of the uniaxial stress. The starting point is the expression of the magnetization given bellow (see (67) from [42]).

$$M = \int_0^\pi \left[\frac{M_s \cos\phi\, e^{\left(\frac{3\chi_0 H}{M_s}\cos\phi + B(\sigma)(\cos^2\phi - 1/3)\right)}}{\int_0^\pi e^{\left(\frac{3\chi_0 H}{M_s}\cos\phi + B(\sigma)(\cos^2\phi - 1/3)\right)}\sin(\phi)d\phi} \sin\phi\, d\phi \right]$$ (31)

where $B(\sigma)$ is:

$$B(\sigma) = 1.5 A_s \lambda_s' \left(\sigma^2 + \sigma \frac{\lambda_s}{\lambda_s'} \right)$$
$$= 1.5 A_s \lambda_s' \left(\left(\sigma - \left(\frac{-\lambda_s}{2\lambda_s'}\right) \right)^2 - \left(\frac{-\lambda_s}{2\lambda_s'}\right)^2 \right).$$ (32)

The quantity $-\lambda_s/2\lambda_s'$ (homogeneous to a stress) is denoted by σ_m. It can be noticed that, for any stress σ, one has $B(\sigma_m + \sigma) = B(\sigma_m - \sigma)$. This shows that independently of the magnetic field, the magnetization as a function of stress is always symmetric with respect to $\sigma = \sigma_m$. Such symmetry is naturally inherited by the relative permeability. Furthermore to prove that μ_r is maximal at σ_m, we first carry out the
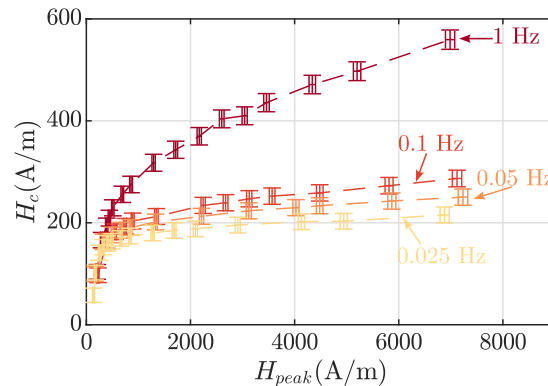

FIGURE 15. Coercive field evolution at several frequency levels.

integration with respect to ϕ in (31) which yields:

$$M = M_s \left[\frac{e^B \left(e^{\frac{3\chi_0 H}{M_s}} - e^{-\frac{3\chi_0 H}{M_s}} \right) e^{\left(\frac{9H^2\chi_0^2}{4M_s^2 B} \right)}}{\sqrt{B\pi} \left(\text{erfi}\left(\sqrt{B} - \frac{3H\chi_0}{2M_s\sqrt{B}} \right) + \text{erfi}\left(\sqrt{B} + \frac{3H\chi_0}{2M_s\sqrt{B}} \right) \right)} - \frac{3H\chi_0}{2M_s B} \right],$$ (33)

where erfi is the imaginary error function given as:

$$\text{erfi}(x) = \frac{2}{\sqrt{\pi}} \int_0^x e^{t^2} dt.$$ (34)

Upon taking the limit of $\partial M/\partial H$ at $H \to 0$ one gets:

$$\mu_r^{anh}(\sigma) = 1 + 3\chi_0 \left(\frac{e^{B(\sigma)}}{\sqrt{B(\sigma)\pi}\,\text{erfi}(\sqrt{B(\sigma)})} - \frac{1}{2B(\sigma)} \right).$$ (35)

This gives an analytical expression of the relative magnetic permeability, in the case of isotropic materials when the uniaxial loading is applied parallel to the magnetic field. By studying the function $\mu_r^{anh}(\sigma)$, one can show that: (a) it is maximal at $\sigma_m = -\lambda_s/2\lambda_s'$, (b) it has $\sigma = \sigma_m$ as an axis of symmetry, (c) it has $\mu_r^{anh} = 1$ as a horizontal asymptote and (d) equals $1 + \chi_0$ for $\sigma = 0$ (using a second-order Taylor series expansion). These characteristics explain the bell shaped curve observed in Fig. 4 and allow an easy identification of λ_s' from the values of λ_s and σ_m.

APPENDIX B
DEFINITION OF THE QUASI-STATIC REGIME

A characterization without stress indicates that a frequency of 1 Hz does not allow a quasi-static assumption for this material sample, as seen in Fig. 15, where a significant change is observed in the coercive field when comparing measurements at 1 Hz and 25 mHz. The remanent induction (Fig. 16) is less sensitive to changes in frequency for 0 MPa. The hysteresis measurements under uniaxial stress are performed considering that the frequency of 25 mHz allows reaching the quasi-static regime. Such a value cannot be considered general since it is dependent on the prescribed waveform for the current, but it was empirically determined as relevant for the measurements shown in this paper.
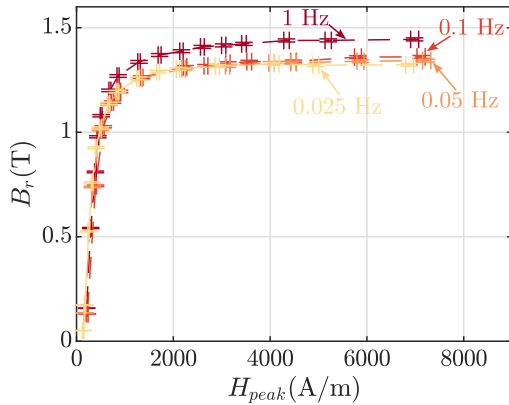
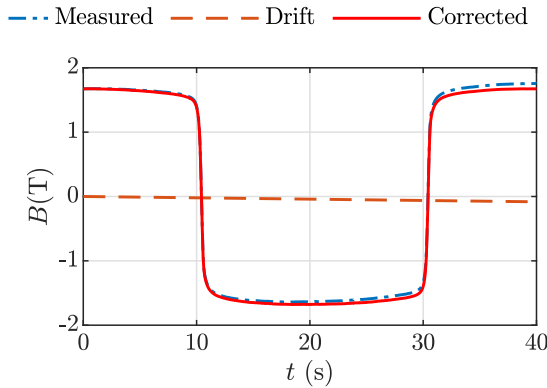**FIGURE 16.** Remanent induction evolution at several frequency levels.

FIGURE 17. Correction of drift in induction after the first magnetization.

APPENDIX C
CORRECTION OF DRIFT IN MAGNETIC INDUCTION

The integration DC drift - or a cumulative offset - in voltage measurements can be related with thermal variation of electronic components [53]. This becomes more problematic with the choice of the frequency of 25 mHz for the input waveform. The drift in the measured induction B_{mes} is linearly corrected with (36), considering the difference between two peaks: in Fig. 17 they are taken as $B_{max}^{(1)}$ at $t = 0$ s and $B_{max}^{(2)}$ at $t = 40$ s, with time difference denoted by Δt.

$$B_{cor} = B_{mes} + \frac{t}{\Delta t}\left(B_{max}^{(1)} - B_{max}^{(2)}\right). \quad (36)$$

APPENDIX D
IDENTIFICATION OF THE PINNING FIELD DISTRIBUTION

The identification of the pinning field distribution was performed following the procedure given in [50], [51]. Starting from the demagnetized state, after the application of a unidirectional magnetic field H_a, the homogenized reversible field is

$$H_{rev}(0 \to H_a) = \int_0^\infty \max(H_a - \kappa, 0)\omega(\kappa)d\kappa = F(H_a), \quad (37)$$

where the max operation indicates that only the cells with $\kappa < H_a$ will be modified. An auxiliary function $F(H)$ is then defined:

$$F(H) \equiv \int_0^H \omega(\kappa)(H - \kappa)d\kappa, \quad (38)$$

with first and second derivatives:

$$\partial_H F(H) = \int_0^H \omega(\kappa)d\kappa$$
$$\partial_H^2 F(H) = \omega(H). \quad (39)$$

From the previous magnetic state, if now the magnetic field is decreased until the coercive field $-H_c$, with $0 < H_c < H_a$, the homogenized reversible field is [50] and [51]:

$$H_{rev}(0 \to H_a \to -H_c) = F(H_a) - 2F\left(\frac{H_a + H_c}{2}\right). \quad (40)$$

Because the magnetic polarization is null at the coercive field $J(H_r(0 \to H_a \to -H_c)) = 0$ [50], [51]:

$$F(H_a) - 2F\left(\frac{H_a + H_c}{2}\right) = 0. \quad (41)$$

Therefore, the identification of $F(H)$ can be performed through experimental measurements of coercive field curve under increasing magnetic field $H_c(H_{peak})$ [50]. The pinning field distribution is evaluated from (39).

The steps to construct $F(H)$ are [50] and [51]:

- Starting from a saturating magnetic field H_s, where $H_c(H_s) = H_c^{max}$, from (38) is observed that $F(H_s) = H_s - H_c^{max}$, with $H_c^{max} = \int_0^{H_s} \kappa\omega(\kappa)d\kappa$.
- Because $H_c(H) < H$:

$$\frac{H + H_c(H)}{2} < H. \quad (42)$$

The strictly decreasing series is defined:

$$H^n = \frac{H^{n-1} + H_c(H^{n-1})}{2} < H^{n-1} \quad (43)$$

with

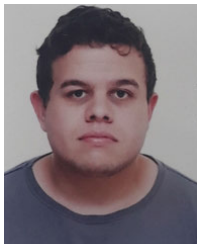$$\frac{F(H^n)}{2} = F\left(H^{n-1}\right). \quad (44)$$

For numerical simulation purposes, a discrete approximation of $\omega(\kappa)$ can be evaluated. The magnetic field is decomposed into N discrete parts and the discrete set $(\omega^k, \kappa^k)_{k=1,\dots,N}$ is [50]:

$$\omega^k = \int_{H^{k-1}}^{H^k} \omega(\kappa)d\kappa = \partial_H F(H^k) - \partial_H F(H^{k-1})$$
$$\kappa^k = \frac{\int_{H^{k-1}}^{H^k} \kappa\omega(\kappa)d\kappa}{\int_{H^{k-1}}^{H^k} \omega(\kappa)d\kappa} = \frac{[H\partial_H F(H) - F(H)]_{H^{k-1}}^{H^k}}{\omega^k}. \quad (45)$$
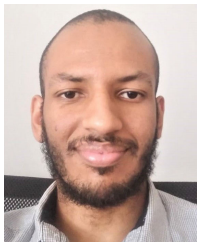
REFERENCES

[1] M. LoBue, C. Sasso, V. Basso, F. Fiorillo, and G. Bertotti, "Power losses and magnetization process in Fe–Si non-oriented steels under tensile and compressive stress," *J. Magn. Magn. Mater.*, vols. 215-216, pp. 124–126, Jun. 2000.

[2] O. Perevertov and R. Schäfer, "Magnetic properties and magnetic domain structure of grain-oriented Fe-3%Si steel under compression," *Mater. Res. Exp.*, vol. 3, no. 9, pp. 1–12, 2016.

[3] U. Aydin, P. Rasilo, F. Martin, A. Belahcen, L. Daniel, A. Haavisto, and A. Arkkio, "Effect of multi-axial stress on iron losses of electrical steel sheets," *J. Magn. Magn. Mater.*, vol. 469, pp. 19–27, Jan. 2019.

[4] K. Yamazaki and H. Takeuchi, "Impact of mechanical stress on characteristics of interior permanent magnet synchronous motors," *IEEE Trans. Ind. Appl.*, vol. 53, no. 2, pp. 963–970, Mar./Apr. 2017.

[5] K. Yamazaki, Y. Sato, M. Domenjoud, and L. Daniel, "Iron loss analysis of permanent-magnet machines by considering hysteresis loops affected by multi-axial stress," *IEEE Trans. Magn.*, vol. 56, no. 1, pp. 1–4, Jan. 2020.

[6] M. J. Sablik, G. Kwun, and G. L. Burkhardt, "Model for the effect of tensile and compressive stress on ferromagnetic hysteresis," *J. Appl. Phys.*, vol. 61, no. 8, pp. 3799–3801, 1987.

[7] M. J. Sablik, G. L. Burkhardt, H. Kwun, and D. C. Jiles, "A model for the effect of stress on the low-frequency harmonic content of the magnetic induction in ferromagnetic materials," *J. Appl. Phys.*, vol. 63, no. 8, pp. 3930–3932, Apr. 1988.

[8] M. J. Sablik, S. W. Rubin, L. A. Riley, D. C. Jiles, D. A. Kaminski, and S. B. Biner, "A model for hysteretic magnetic properties under the application of noncoaxial stress and field," *J. Appl. Phys.*, vol. 74, no. 1, pp. 480–488, Jul. 1993.

[9] A. Dorfmann and R. W. Ogden, "Magnetoelastic modelling of elastomers," *Eur. J. Mech.-A/Solids*, vol. 22, no. 4, pp. 497–507, Jul. 2003.

[10] K. Fonteyn, A. Belahcen, R. Kouhia, P. Rasilo, and A. Arkkio, "FEM for directly coupled magneto-mechanical phenomena in electrical machines," *IEEE Trans. Magn.*, vol. 46, no. 8, pp. 2923–2926, Aug. 2010.

[11] P. Rasilo, D. Singh, U. Aydin, F. Martin, R. Kouhia, A. Belahcen, and A. Arkkio, "Modeling of hysteresis losses in ferromagnetic laminations under mechanical stress," *IEEE Trans. Magn.*, vol. 52, no. 3, pp. 1–4, Mar. 2016.

[12] U. Aydin, P. Rasilo, F. Martin, D. Singh, L. Daniel, A. Belahcen, R. Kouhia, and A. Arkkio, "Modeling the effect of multiaxial stress on magnetic hysteresis of electrical steel sheets: A comparison," *IEEE Trans. Magn.*, vol. 53, no. 6, pp. 1–4, Jun. 2017.

[13] J. V. Leite, N. Sadowski, P. Kuo-Peng, and A. Benabou, "Minor loops calculation with a modified Jiles–Atherton hysteresis model," *J. Microw., Optoelectron. Electromagn. Appl.*, vol. 8, no. 1, pp. 49S–55S, 2009.

[14] S. E. Zirka, Y. I. Moroz, R. G. Harrison, and K. Chwastek, "On physical aspects of the Jiles–Atherton hysteresis models," *J. Appl. Phys.*, vol. 112, no. 4, Aug. 2012, Art. no. 043916.

[15] A. Bergqvist and G. Engdahl, "A stress-dependent magnetic Preisach hysteresis model," *IEEE Trans. Magn.*, vol. 27, no. 6, pp. 4796–4798, Nov. 1991.

[16] G. V. Bolshakov and A. J. Lapovok, "A Preisach model for magnetoelastic hysteresis," *J. Magn. Magn. Mater.*, vol. 162, no. 1, pp. 112–116, Sep. 1996.

[17] A. Sipeky and A. Ivanyi, "Preisach-type stress-dependent magnetic vector hysteresis model," *Phys. B, Condens. Matter*, vol. 403, nos. 2–3, pp. 491–495, Feb. 2008.

[18] D. Mukherjee and K. Danas, "An evolving switching surface model for ferromagnetic hysteresis," *J. Appl. Phys.*, vol. 125, no. 3, pp. 1–19, 2019.

[19] D. Mukherjee, M. Rambausek, and K. Danas, "An explicit dissipative model for isotropic hard magnetorheological elastomers," *J. Mech. Phys. Solids*, vol. 151, pp. 1–35, Jan. 2021.

[20] L. Daniel, O. Hubert, N. Buiron, and R. Billardon, "Reversible magnetoelastic behavior: A multiscale approach," *J. Mech. Phys. Solids*, vol. 56, no. 3, pp. 1018–1042, Mar. 2008.

[21] D. Vanoost, S. Steentjes, J. Peuteman, G. Gielen, H. De Gersem, D. Pissoort, and K. Hameyer, "Magnetic hysteresis at the domain scale of a multi-scale material model for magneto-elastic behaviour," *J. Magn. Magn. Mater.*, vol. 414, pp. 168–179, Sep. 2016.

[22] L. Bernard, B. J. Mailhé, N. Sadowski, N. J. Batistela, and L. Daniel, "Multiscale approaches for magneto-elasticity in device simulation," *J. Magn. Magn. Mater.*, vol. 487, pp. 1–13, Oct. 2019.

[23] W. D. Armstrong, "Magnetization and magnetostriction processes in $Tb_{(0.27-0.30)}Dy_{(0.73-0.70)}Fe_{(1.9-2.0)}$," *J. Appl. Phys.*, vol. 81, no. 5, pp. 2321–2326, Mar. 1997.

[24] L. Bernard, X. Mininger, L. Daniel, G. Krebs, F. Bouillault, and M. Gabsi, "Effect of stress on switched reluctance motors: A magneto-elastic finite-element approach based on multiscale constitutive laws," *IEEE Trans. Magn.*, vol. 47, no. 9, pp. 2171–2178, Sep. 2011.

[25] L. Daniel, O. Hubert, and M. Rekik, "A simplified 3-D constitutive law for magnetomechanical behavior," *IEEE Trans. Magn.*, vol. 51, no. 3, pp. 1–4, Mar. 2015.

[26] L. Daniel, "An analytical model for the effect of multiaxial stress on the magnetic susceptibility of ferromagnetic materials," *IEEE Trans. Magn.*, vol. 49, no. 5, pp. 2037–2040, May 2013.

[27] L. Daniel, "An analytical model for the magnetostriction strain of ferromagnetic materials subjected to multiaxial stress," *Eur. Phys. J. Appl. Phys.*, vol. 83, no. 3, pp. 1–6, 2018.

[28] S. Ito, T. Mifune, T. Matsuo, and C. Kaido, "Macroscopic magnetization modeling of silicon steel sheets using an assembly of six-domain particles," *J. Appl. Phys.*, vol. 117, no. 17, pp. 1–4, 2015.

[29] S. Ito, T. Mifune, T. Matsuo, C. Kaido, Y. Takahashi, and K. Fujiwara, "Simulation of the stress dependence of hysteresis loss using an energy-based domain model," *AIP Adv.*, vol. 8, no. 4, pp. 1–7, 2018.

[30] L. Daniel, M. Rekik, and O. Hubert, "A multiscale model for magneto-elastic behaviour including hysteresis effects," *Arch. Appl. Mech.*, vol. 84, nos. 9–11, pp. 1307–1323, Oct. 2014.

[31] L. Bernard and L. Daniel, "Effect of stress on magnetic hysteresis losses in a switched reluctance motor: Application to stator and rotor shrink fitting," *IEEE Trans. Magn.*, vol. 51, no. 9, pp. 1–13, Sep. 2015.

[32] L. Bernard, B. J. Mailhé, S. L. Avila, L. Daniel, N. J. Batistela, and N. Sadowski, "Magnetic hysteresis under compressive stress: A multiscale-Jiles–Atherton approach," *IEEE Trans. Magn.*, vol. 56, no. 2, pp. 1–4, Feb. 2020.

[33] B. S. Ram, A. P. S. Baghel, S. V. Kulkarni, K. Chwastek, and L. Daniel, "A hybrid product-multi-scale model for magneto-elastic behavior of soft magnetic materials," *Phys. B, Condens. Matter.*, vol. 571, pp. 301–306, Oct. 2019.

[34] B. Sai Ram, A. P. S. Baghel, S. V. Kulkarni, L. Daniel, and I. C. Nlebedim, "A frequency-dependent scalar magneto-elastic hysteresis model derived using multi-scale and Jiles–Atherton approaches," *IEEE Trans. Magn.*, vol. 56, no. 3, pp. 1–5, Mar. 2020.

[35] W. D. Armstrong, "An incremental theory of magneto-elastic hysteresis in pseudo-cubic ferro-magnetostrictive alloys," *J. Magn. Magn. Mater.*, vol. 263, nos. 1–2, pp. 208–218, 2003.

[36] P. G. Evans and M. J. Dapino, "Efficient magnetic hysteresis model for field and stress application in magnetostrictive Galfenol," *J. Appl. Phys.*, vol. 107, no. 6, 2010, Art. no. 063906.

[37] C. Miehe and G. Ethiraj, "A geometrically consistent incremental variational formulation for phase field models in micromagnetics," *Comput. Methods Appl. Mech. Eng.*, vols. 245–246, pp. 331–347, Oct. 2012.

[38] A. Sridhar, M.-A. Keip, and C. Miehe, "Homogenization in micromagneto-mechanics," *Comput. Mech.*, vol. 58, no. 1, pp. 151–169, Jul. 2016.

[39] F. Henrotte, A. Nicolet, and K. Hameyer, "An energy-based vector hysteresis model for ferromagnetic materials," *COMPEL-Int. J. Comput. Math. Elect. Electron. Eng.*, vol. 25, no. 1, pp. 71–80, 2006.

[40] V. François-Lavet, F. Henrotte, L. Stainier, L. Noels, and C. Geuzaine, "An energy-based variational model of ferromagnetic hysteresis for finite element computations," *J. Comput. Appl. Math.*, vol. 246, pp. 243–250, Jul. 2013.

[41] G. T. Houlsby and A. M. Puzrin, "A thermomechanical framework for constitutive models for rate-independent dissipative materials," *Int. J. Plasticity*, vol. 16, no. 9, pp. 1017–1047, Aug. 2000.

[42] O. Hubert, "Multiscale magneto-elastic modeling of magnetic materials including isotropic second order stress effect," *J. Magn. Magn. Mater.*, vol. 491, pp. 1–16, Jan. 2019.

[43] L. Daniel and O. Hubert, "Equivalent stress criteria for the effect of stress on magnetic behavior," *IEEE Trans. Magn.*, vol. 46, no. 8, pp. 3089–3092, Aug. 2010.

[44] W. Zhao, S. Wang, X. Xie, X. Zhou, and L. Liu, "A simplified multiscale magneto-mechanical model for magnetic materials," *J. Magn. Magn. Mater.*, vol. 526, pp. 1–9, May 2021.

[45] N. Buiron, L. Hirsinger, and R. Billardon, "A multiscale model for magneto-elastic couplings," *J. Phys. IV*, vol. 9, pp. 187–196, Sep. 1999.

[46] L. Daniel and N. Galopin, "A constitutive law for magnetostrictive materials and its application to Terfenol-D single and polycrystals," *Eur. Phys. J. Appl. Phys.*, vol. 42, no. 2, pp. 153–159, May 2008.

[47] L. Prigozhin, V. Sokolovsky, J. W. Barrett, and S. E. Zirka, "On the energy-based variational model for vector magnetic hysteresis," *IEEE Trans. Mag.*, vol. 52, no. 12, pp. 1–11, Dec. 2016.

[48] M. Domenjoud, É. Berthelot, N. Galopin, R. Corcolle, Y. Bernard, and L. Daniel, "Characterization of giant magnetostrictive materials under static stress: Influence of loading boundary conditions," *Smart Mater. Struct.*, vol. 28, no. 9, pp. 1–10, 2019.

[49] L. Daniel and M. Domenjoud, "Anhysteretic magneto-elastic behaviour of Terfenol-D: Experiments, multiscale modelling and analytical formulas," *Materials*, vol. 14, no. 18, pp. 1–12, 2021.

[50] F. Henrotte, S. Steentjes, K. Hameyer, and C. Geuzaine, "Iron loss calculation in steel laminations at high frequencies," *IEEE Trans. Magn.*, vol. 50, no. 2, pp. 333–336, Feb. 2014.

[51] K. Jacques, S. Steentjes, C. Geuzaine, and K. Hameyer, "Representation of microstructural features and magnetic anisotropy of electrical steels in an energy-based vector hysteresis model," *AIP Adv.*, vol. 8, no. 4, pp. 1–10, 2018.

[52] D. Singh, F. Martin, P. Rasilo, and A. Belachen, "Magnetomechanical model for hysteresis in electrical steel sheet," *IEEE Trans. Magn.*, vol. 52, no. 11, pp. 1–9, Nov. 2016.

[53] J. A. Garcia and M. Rivas, "A quasi-static magnetic hysteresis loop measurement system with drift correction," *IEEE Trans. Magn.*, vol. 42, no. 1, pp. 15–17, Jan. 2006.

LUIZ GUILHERME DA SILVA received the M.Sc. degree in electrical engineering from the Universidade Federal de Santa Catarina, Florianópolis, Brazil, in 2020. He is currently pursuing the Ph.D. degree in electrical engineering with the Group of Electrical Engineering of Paris (GeePs), CentraleSupélec, Université Paris-Saclay. His research interests include the modeling and characterization of the coupled magnetomechanical behavior in ferromagnetic materials and numerical methods for electromagnetic devices simulation.

ABDELLAHI ABDERAHMANE received the degree in mechanical engineering from El Manar University, Tunis, Tunisia, in 2016, and the master's degree in acoustical engineering and the Ph.D. degree in electrical engineering from Paris-Saclay University, Paris, France, in 2017 and 2021, respectively. He is currently a Postdoctoral Researcher at the Group of Electrical Engineering of Paris (GeePs), Paris-Saclay University. His research interests include nondestructive testing, tomography imaging, and ferromagnetic materials characterization.

MATHIEU DOMENJOUD received the M.Sc. degree in electrical engineering from François-Rabelais University, Tours, France, and the Ph.D. degree in electrical engineering with a focus on the characterization of electro-acoustic properties of piezoelectric structures under electrical and mechanical stress from the GREMAN Laboratory, François-Rabelais University, in 2012. He became an Assistant Professor with the IUT of Cachan (Université Paris-Saclay, in 2012, previously Université Paris-Sud) and joined the Group of Electrical Engineering of Paris (GeePs, previously LGEP), France. His research interests include the characterization of electro-magneto-mechanical couplings, the definition of constitutive laws by phenomenological approaches, and the prediction of such coupled phenomena by considering multiscale methods.

LAURENT BERNARD received the joint Ph.D. degree in electrical engineering from the Ecole Centrale de Lyon, France, and the Universidade Federal de Minas Gerais, Belo Horizonte, Brazil, in 2007. From 2007 to 2015, he worked as a Research Engineer with the Centre National de la Recherche Scientifique (CNRS), Group of Electrical Engineering of Paris (GeePs), Gif-sur-Yvette, France. Since 2015, he has been a Professor with the Department of Electrical Engineering, Universidade Federal de Santa Catarina, Florianópolis, Brazil. His research interests include mesh-based numerical methods and advanced modeling of material behavior for electromagnetics and coupled magnetomechanical problems.

LAURENT DANIEL received the Ph.D. degree from the Ecole Normale Supérieure de Cachan, Cachan, France, in 2003, and the Habilitation degree in physics from Université Paris-Sud, Orsay, France, in 2011. Since 2015, he has been a Full Professor with the CentraleSupélec, Université Paris-Saclay, Gif-sur-Yvette, France. His research interests include, within the Group of Electrical Engineering of Paris (GeePs), are dedicated to electromechanical and magnetomechanical couplings in materials for electrical engineering applications. He is notably involved in the definition of multiscale methods for the prediction of such coupled phenomena and in the development of dedicated experimental characterization setups. Since 2014, he has been the Director of the Automotive Mechatronics Chair, a partnership between CentraleSupélec, Esigelec, and Automotive Company Forvia.

• • •

COMMENTS AND CORRECTIONS

Corrections to "An Extension of the Vector-Play Model to the Case of Magneto-Elastic Loadings"

LUIZ GUILHERME DA SILVA [1,2,3], **ABDELLAHI ABDERAHMANE** [1,2],
MATHIEU DOMENJOUD [1,2], **LAURENT BERNARD** [3],
AND LAURENT DANIEL [1,2]

[1] Laboratoire de Génie Electrique et Electronique de Paris, CentraleSupélec, CNRS, Université Paris-Saclay, 91192 Gif-sur-Yvette, France
[2] Laboratoire de Génie Electrique et Electronique de Paris, CNRS, Sorbonne Université, 75252 Paris, France
[3] GRUCAD/EEL/CTC, Federal University of Santa Catarina (UFSC), Florianópolis 88040-900, Brazil

Corresponding author: Luiz Guilherme da Silva (luiz.dasilva@geeps.centralesupelec.fr)

There is an error in the above article [1] when the components of the second order magnetostriction strain tensor $\epsilon_\alpha^{\mu(2)}$ are introduced in section II.B, just before equation (14). It is stated that, in the case of a uniaxial stress tensor applied parallel to the magnetic field (direction 1), the only non-null component of $\epsilon_\alpha^{\mu(2)}$ is $\epsilon_{\alpha_{11}}^{\mu(2)}$. Although the expression given for $\epsilon_{\alpha_{11}}^{\mu(2)}$ by (14) in [1] is correct, the 11 component is not the only non-null component of $\epsilon_\alpha^{\mu(2)}$. The general expression of $\epsilon_\alpha^{\mu(2)}$ is given by equation (1) below:

$$
\epsilon_\alpha^{\mu(2)} = -\frac{\partial g_\alpha^{el(2)}}{\partial \boldsymbol{\sigma}}
$$
$$
= \frac{9}{2}\lambda_s' \sigma_{eq}\left[\left(\vec{\alpha}\otimes\vec{\alpha}-\frac{1}{3}\boldsymbol{I}\right):\left(\vec{h}\otimes\vec{h}\right)\right]\left(\vec{h}\otimes\vec{h}-\frac{1}{3}\boldsymbol{I}\right)
$$
$$
\tag{1}
$$

The particular case considered in [1], with $\vec{h} = [1\ 0\ 0]^t$ and $\boldsymbol{\sigma} = \sigma_{11}\left(\vec{h}\otimes\vec{h}\right)$ yields:

$$
\epsilon_{\alpha_{11}}^{\mu(2)} = 3\lambda_s'\sigma_{11}\left(\alpha_1{}^2 - \frac{1}{3}\right)
$$
$$
\epsilon_{\alpha_{22}}^{\mu(2)} = \epsilon_{\alpha_{33}}^{\mu(2)} = -\frac{3}{2}\lambda_s'\sigma_{11}\left(\alpha_1{}^2 - \frac{1}{3}\right)
$$
$$
\epsilon_{\alpha_{23}}^{\mu(2)} = \epsilon_{\alpha_{13}}^{\mu(2)} = \epsilon_{\alpha_{12}}^{\mu(2)} = 0
\tag{2}
$$

This error does not affect the following calculations presented in the article.

REFERENCES

[1] L. G. D. Silva, A. Abderahmane, M. Domenjoud, L. Bernard, and L. Daniel, "An extension of the vector-play model to the case of magneto-elastic loadings," *IEEE Access*, vol. 10, pp. 126674–126686, 2022.

• • •